

Mesoscale modeling of amorphous metals by shear transformation zone dynamics

Eric R. Homer, Christopher A. Schuh *

Department of Materials Science and Engineering, Massachusetts Institute of Technology, 77 Massachusetts Avenue, Cambridge, MA 02139, USA

Received 23 December 2008; received in revised form 10 February 2009; accepted 24 February 2009

Available online 28 March 2009

Abstract

A new mesoscale modeling technique for the thermo-mechanical behavior of metallic glasses is proposed. The modeling framework considers the shear transformation zone (STZ) as the fundamental unit of deformation, and coarse-grains an amorphous collection of atoms into an ensemble of STZs on a mesh. By employing finite element analysis and a kinetic Monte Carlo algorithm, the modeling technique is capable of simulating glass processing and deformation on time and length scales greater than those usually attainable by atomistic modeling. A thorough explanation of the framework is presented, along with a specific two-dimensional implementation for a model metallic glass. The model is shown to capture the basic behaviors of metallic glasses, including high-temperature homogeneous flow following the expected constitutive law, and low-temperature strain localization into shear bands. Details of the effects of processing and thermal history on the glass structure and properties are also discussed.

© 2009 Acta Materialia Inc. Published by Elsevier Ltd. All rights reserved.

Keywords: Metallic glass; Shear bands; Micromechanical modeling; Activated processes; Shear transformation zone

1. Introduction

Amorphous metals exhibit a rich diversity of deformation behavior, with significant differences from classic crystalline deformation behavior [1,2]. For example, at high homologous temperatures amorphous metals behave as supercooled liquids and display homogeneous deformation that is Newtonian over a broad range of low stresses. At somewhat higher stresses their rheology becomes non-Newtonian, but follows an exponential stress dependence rather than the power-law common to crystalline metals. On the other hand, at low temperatures and high stresses, amorphous metals deform in a highly inhomogeneous fashion where plastic strain tends to localize into nanoscale shear bands that encourage catastrophic failure.

Central to understanding this diverse behavior in amorphous metals are the deformation mechanisms that act on a microscopic level. The shear transformation zone (STZ)

proposed by Argon [3] has emerged as a useful mechanistic picture in which the unit process of deformation is a collective motion of a few atoms that rearrange to achieve a characteristic shear strain, γ_0 , under an applied shear stress, as shown in Fig. 1. The STZ is viewed as a stress-biased, thermally activated event, permitting simple rate laws for STZ activation to be written in terms of state variables, including stress, temperature and local structural order parameters such as free volume [4]. One advantage of defining a unit STZ process in this way is that by appropriately modeling the dynamics of these events, one may overlook the local details of individual atomic motions, while still capturing the fundamental physics of deformation. For example, by assuming that STZs operate independently of one another, one can readily calculate the average behavior of STZs in the system. This approach yields an analytical solution for the steady-state flow law of a homogeneously deforming amorphous metal, with a hyperbolic-sine stress dependence that is commonly seen in experiments [1,5].

On the other hand, the more complex and interesting behaviors associated with shear localization and fracture,

* Corresponding author.

E-mail address: schuh@MIT.EDU (C.A. Schuh).

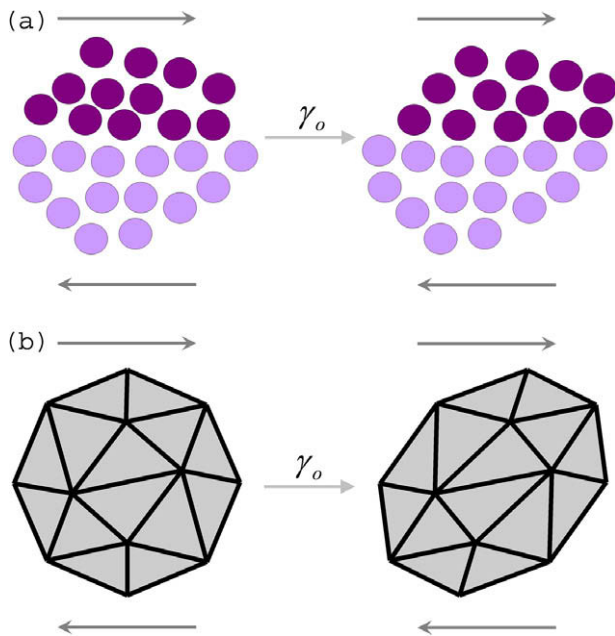


Fig. 1. (a) Shear transformation zone, or STZ, where several dozen atoms shear inelastically under an applied shear stress; (b) an idealization of an STZ on a continuum mesh.

for example, require the collective action of many STZs, which may no longer be assumed to operate independently of one another. In this situation, the rate law for STZ activation must be supplemented with details of how STZs interact, and how their operation redistributes stress and free volume in the system [4]. Without a priori knowledge of STZ interactions, there is as yet no clear connection between local atomic motions and the macroscopic deformation behavior of amorphous metals undergoing shear localization [6].

A further difficulty for modeling strain localization in amorphous metals is that the process involves time and length scales that span many orders of magnitude. For example, local atomic motions, including STZ activation, occur on a timescale of about 10^{-12} – 10^{-11} s, while shear band formation occurs over periods of 10^{-5} – 10^{-3} s in experiments [7,8]. Similarly, shear band thickness is usually found to be of order 10^{-8} – 10^{-7} m [9,10], with typical shear offsets that can be much larger, 10^{-6} m or greater [11,12]; both of these values are much larger than the size of an STZ at $\sim 10^{-10}$ – 10^{-9} m [13,14]. These facts suggest that shear band formation involves a slow cooperative process involving a great many STZs.

This disparity in time and length scales creates difficulties for clean experimentation, and even more for modeling the full range of glass behaviors under experimentally relevant conditions. For example, molecular dynamics simulations exquisitely track atomic motion [15–25], but are intrinsically limited to small length scales and, more importantly, to very short time scales. This restricts their ability to capture large-scale events that occur on long time scales, including glass formation by cooling from the melt at

experimental rates. Although shear localization is seen in many atomistic simulations of amorphous systems [24,26–31], it generally requires very driven systems that cannot be easily compared to experiments. On the other hand, continuum simulations have the ability to access much larger system sizes and longer time scales through the development of constitutive relations and the use of finite element analysis (FEA) [32,33]. These models are especially powerful for modeling complex geometries with realistic boundary conditions, but they are limited by the constitutive relationships on which they are constructed, which can only capture the specific physics that they have been designed to model.

In order to access deformation behavior intermediate to these two modeling techniques, there is a need for meso-scale models based upon an ensemble of characteristic events such as the STZ. A coarse-graining approach of this type was proposed by Bulatov and Argon [34], who developed a lattice STZ model in which each lattice element represented a single potential STZ. The activation or shearing of any single STZ led to the redistribution of stress and strain in the system, which in turn affected the rate of activation for subsequent STZ operations. The selection of STZs for activation and the time evolution of the system were controlled through a kinetic Monte Carlo algorithm [34–36]. This model reproduced both homogeneous and inhomogeneous modes of deformation and accessed significant time scales. One clear limitation of this model, however, involved the use of a fixed lattice geometry, which cannot capture the spatial evolution, or shape change, of the system. In addition, Bulatov and Argon's use of Green's functions to determine the stress and strain distributions in the system improved computational efficiency but limited their ability to model complex geometries and stress states.

The purpose of this paper is to develop a new mesoscale modeling technique that we term “STZ dynamics” modeling. This approach considers STZ activation as a stochastic, stress-biased, thermally activated event which obeys a specific rate law and uses the kinetic Monte Carlo method to control the evolution of the system. We employ FEA to solve the elastic strain distribution in the system, by which the STZs communicate with one another. In this manner, we are able to access longer time and length scales than those associated with atomic motions. Our model takes its inspiration from the lattice model of Bulatov and Argon [34], but expands upon it in the sense that our use of FEA permits arbitrary shape changes, complex geometries and boundary conditions, greater freedom in the definition and activation of STZs, and a close connection to experimental conditions. In this paper, we present our basic methodology, then proceed to develop a specific two-dimensional implementation as a demonstration of the method. We explore the thermal response and effects of processing, the rheological nature of deformation at high temperatures and shear localization at low temperatures. Lastly, a compilation of data from many simulations is

used to construct a deformation map for a model metallic glass.

2. Modeling framework

2.1. Shear transformation zones

We model an amorphous material as an elastic continuum consisting of an ensemble of potential STZs defined on a mesh. In essence, we substitute a continuum mesh for collections of atoms, as shown schematically in Fig. 1. We treat the shearing of an STZ as an Eshelby inclusion problem [37], as proposed by Argon in his calculation of the activation energy barrier for shearing of an STZ [3,38]. In this approach, an STZ undergoes a stress-free strain transformation, after which both the STZ and surrounding matrix elastically accommodate the transformation strain. The activation energy barrier as determined by Argon [3,38] is

$$\Delta F = \left[\frac{7-5\nu}{30(1-\nu)} - \frac{2(1+\nu)}{9(1-\nu)}\beta^2 + \frac{1}{2\gamma_o} \cdot \frac{\hat{\tau}}{\mu(T)} \right] \cdot \mu(T) \cdot \gamma_o^2 \cdot \Omega_o, \quad (1)$$

where the first term represents the strain energy of an STZ sheared by the characteristic shear strain, γ_o (which is of order ~ 0.1). The second term represents the strain energy for a temporary dilatation to allow the atoms to rearrange into the sheared position where β (of order ~ 1) represents the ratio of STZ dilatation during transformation to the characteristic shear strain γ_o . The third term represents the energy required to freely shear an STZ, with $\hat{\tau}$ equal to the peak interatomic shear resistance between atoms. The material properties ν and $\mu(T)$, respectively, represent Poisson's ratio and the temperature-dependent shear modulus of both the STZ and surrounding matrix. Finally, the STZ volume is given by Ω_o , with the product $\gamma_o \cdot \Omega_o$ equal to the activation volume of the STZ.

In our approach, the finite element mesh and the definition of the STZs on the mesh are selected with the following characteristics in mind:

- The geometrical shape of the STZ in the mesh should resemble that observed in simulations and models, roughly spherical in three dimensions or circular in two [3,14,25,39,40].
- Each individual STZ should be represented by a sufficient number of elements to accurately resolve the stress and strain distributions in the mesh.
- Elements that belong to one STZ should be able to participate in other potential STZs, just as atoms may participate in various different STZs.

One simple implementation that achieves these criteria in two dimensions is a triangular mesh with STZs bound to the nodes and elements of the mesh. For example, STZs may be centered on nodes of the mesh and incorporate a

number of surrounding elements extending radially outwards. This is illustrated in Fig. 2a, where 6-, 24- and 54-element STZs are defined on a central node and include, respectively, one, two and three elements extending radially outwards. Alternatively, STZs may be centered on a single element and incorporate elements extending radially outwards. An example is shown in Fig. 2a for a 13-element STZ extending one element radially outwards to include elements which share common nodes. The details of the STZ definition become important in the accuracy of stress and strain field calculations, and will be discussed in a later section. Finally, while in principle one might define an ensemble of STZs with different characteristic volumes, Ω_o , based on the local size of the elements included in each potential STZ, the simplest approach is to assign a single value of Ω_o to all the STZs in the mesh, as we shall do in the present implementation.

The last desired STZ characteristic that is satisfied by the STZs defined on the triangular mesh is that elements in the mesh will be able to participate in multiple STZs. Provided that STZs comprise more than a single element, this condition is naturally achieved, as illustrated in Fig. 2b, where three potential STZs, each of 13 elements, are highlighted on an irregular triangular mesh. At any given time step, the elements in the overlap region between

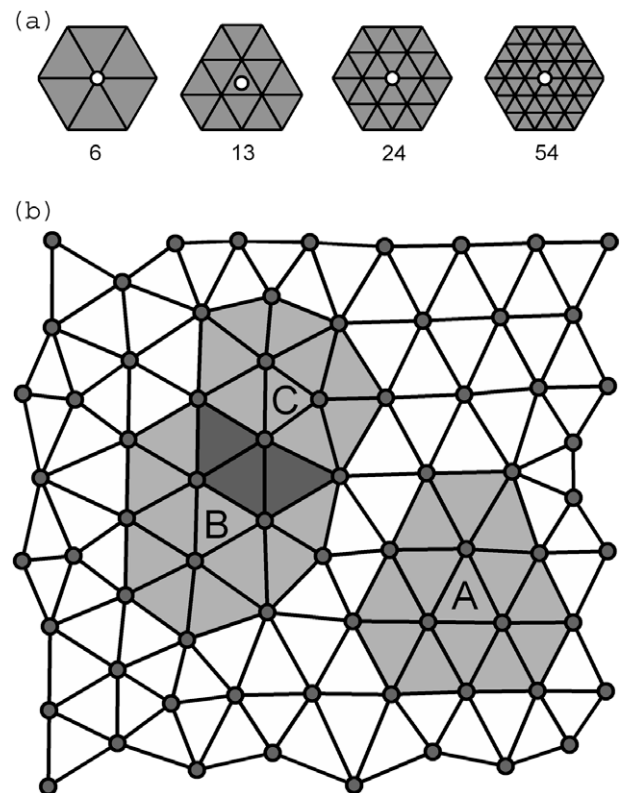


Fig. 2. (a) Representation of several possible STZ definitions on a triangular lattice. (b) Irregular triangular mesh with 13-element potential STZs highlighted and denoted by A, B and C; B and C show how individual elements in the mesh can be activated by different STZs.

potential STZs B and C can participate in either event (and others not shown).

2.2. Kinetic Monte Carlo

The activation rate law of a single potential STZ is given by

$$\dot{s} = v_o \cdot \exp\left(-\frac{\Delta F - \tau \cdot \gamma_o \cdot \Omega_o}{kT}\right), \quad (2)$$

where \dot{s} is the STZ activation rate, ΔF is the local energy given in Eq. (1) for an STZ shearing in the fashion shown in Fig. 1. The local shear stress and temperature are represented by τ and T , respectively. Boltzmann's constant is given by k , and v_o represents the attempt frequency along the reaction pathway, which is of the order of the Debye frequency.

The activation rate defined in Eq. (2), however, only gives the rate for an STZ attempting to shear in one direction. In two dimensions, the rate for an STZ attempting to shear in N different directions around a circle is given by

$$\dot{s} = \frac{v_o}{N} \cdot \sum_{n=1}^N \exp\left(-\frac{\Delta F - \tau_{\max} \cdot \sin\left(\phi + 2\pi \frac{n}{N}\right) \cdot \gamma_o \cdot \Omega_o}{kT}\right), \quad (3)$$

where τ_{\max} is the maximum in-plane shear stress and ϕ is the angle to the current stress state in Mohr space for the given STZ. If Eq. (3) is simplified and the discrete summation is converted to a continuous integral by letting N go to infinity, we have

$$\dot{s} = \frac{v_o}{2\pi} \cdot \exp\left(-\frac{\Delta F}{kT}\right) \cdot \int_0^{2\pi} \exp\left(\frac{\tau_{\max} \cdot \sin(\theta) \cdot \gamma_o \cdot \Omega_o}{kT}\right) d\theta, \quad (4)$$

which evaluates to a modified Bessel function of the first kind, of order zero

$$\dot{s} = v_o \cdot \exp\left(-\frac{\Delta F}{kT}\right) \cdot I_0\left(\frac{\tau_{\max} \cdot \gamma_o \cdot \Omega_o}{kT}\right). \quad (5)$$

Eqs. (4) and (5) integrate the value of the shear stress as we traverse the circle in Mohr space for the given value of the shear stress as defined by $\exp(\tau_{\max} \cdot \sin(\theta))$ for θ on the interval $[0^\circ, 360^\circ)$. Thus, Eqs. (4) and (5) are able to determine the rate for shearing a single STZ in a continuum of directions around a circle, based upon the local stress and temperature of the STZ. The form of Eq. (5) is especially convenient for evaluating the integral computationally.

The kinetic Monte Carlo (KMC) algorithm [34,41,42] can be used to evolve an ensemble of STZs governed by Eqs. (1) and (5), where each STZ may experience a different local temperature and stress state, by repeating the following steps:

1. Calculate and form a list of activation rates, \dot{s}_i , for each of the $i = 1, \dots, N$ STZs in the ensemble, based on the current state of the system.

2. Calculate the cumulative activation rate, \dot{s}_T , for all STZs and normalize each individual rate by \dot{s}_T

$$\eta_i = \dot{s}_i / \dot{s}_T, \quad (6)$$

such that

$$\sum_i \eta_i = 1. \quad (7)$$

3. Generate two random numbers, ξ_1 and ξ_2 , uniformly distributed on the interval $[0, 1)$.

4. Update the elapsed system time with the residence time for the current configuration calculated according to $\Delta t = -\ln \xi_1 / \dot{s}_T$.

5. Select a single STZ by first defining the cumulative fraction of STZ rates up to and including the rate of STZ j by

$$H_j = \sum_{i=1}^j \eta_i, \quad (9)$$

and then use the random number, ξ_2 , to find the STZ which satisfies

$$H_{k-1} < \xi_2 \leq H_k. \quad (10)$$

When listed in a successive fashion, ξ_2 falls on the subinterval η_k in the list of normalized STZ rates, as illustrated in Fig. 3a.

6. To select the angle at which to shear the STZ, we first define the value η' , which represents the magnitude by which ξ_2 overlaps the subinterval of the selected STZ, η_k , as illustrated in Fig. 3b:

$$\eta' = \xi_2 - H_{k-1}. \quad (11)$$

The overlap, η' , is then used to determine the integration limit which satisfies the equality

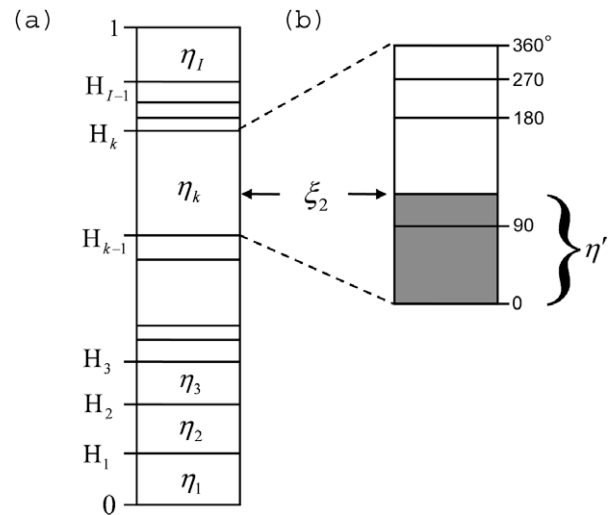


Fig. 3. Schematic of the kinetic Monte Carlo STZ selection procedure: (a) how the random number ξ_2 can be used to select a single STZ for activation from a list of normalized individual STZ rates, $\eta_1, \eta_2, \eta_3, \dots, \eta_i$; (b) the determination of the overlap, η' , between ξ_2 and η_j (as defined in Eq. (11)), which selects the angle of shear of the STZ.

$$\eta' = \frac{1}{s_k} \cdot \frac{v_o}{2\pi} \exp\left(-\frac{\Delta F}{kT}\right) \int_0^{\theta'} \exp\left(\frac{\tau_{\max} \cdot \sin(\theta) \cdot \gamma_o \cdot \Omega_0}{kT}\right) d\theta. \quad (12)$$

The integration limit θ' from Eq. (12) and the angle to the current stress state ϕ can then be used to define the angle of shear in real space, relative to a state of pure shear, by

$$\omega = (\phi - \theta')/2. \quad (13)$$

7. Apply a shear shape distortion to the selected STZ of the form:

$$\begin{bmatrix} \varepsilon_{11} \\ \varepsilon_{22} \\ \gamma_{12} \end{bmatrix} = \begin{bmatrix} \frac{1}{2}\gamma_o \sin(2\omega) \\ -\frac{1}{2}\gamma_o \sin(2\omega) \\ \gamma_o \cos(2\omega) \end{bmatrix}, \quad (14)$$

and subsequently calculate the stress and strain distributions of the new configuration.

The KMC algorithm can be repeated for an arbitrary number of STZ operations and is efficient because every iteration guarantees a transition. The stochastic nature of the processes will produce a realistic outcome if the rates governing the individual events are correct.

While most of the steps listed above are standard to any KMC algorithm, steps five and six deserve further explanation. In the list of normalized STZ rates of Fig. 3a, some subintervals are larger than others, since some STZs experience higher stress than others. Strictly speaking, such STZs experience higher values of λ :

$$\lambda = \frac{\tau_{\max} \cdot \gamma_o \cdot \Omega_0}{kT}, \quad (15)$$

which governs the STZ activation rate (cf. Eq. (5)) and dictates the width of the subinterval η_i . Thus, when selecting the STZ with the random number ξ_2 , the larger subintervals have a higher probability of being selected, giving preference to events that occur on shorter time scales.

The value of λ also impacts the choice of the STZ shearing angle, as a result of the exponential dependence of λ in Eq. (4). This is illustrated by the non-uniform subintervals in Fig. 3b. A more accurate representation of this effect can be seen by calculating the values of η' as determined for different ratios of λ where the integral in Eq. (12) is evaluated from 0 to θ' for a range of θ' on the interval $[0^\circ, 360^\circ]$. The result is plotted as a function of the integration limit θ' in Fig. 4a, where the arrows on the plot point from smaller to larger values of λ (i.e. from states of lower stress/higher temperature to states of higher stress/lower temperature). It can be seen that for small values of λ the curve is linear, meaning that a random number will uniformly select the angle θ' ; at high temperatures or low stress levels there is no preference for the shearing direction of the STZ. For large values of λ , however, the trend in Fig. 4a is sigmoidal, and most randomly selected numbers will preferentially select shearing angles near 90° – the angle of maximum shear in Mohr space. Thus, at low temperatures and/or high stresses, the local stress state biases the STZ into

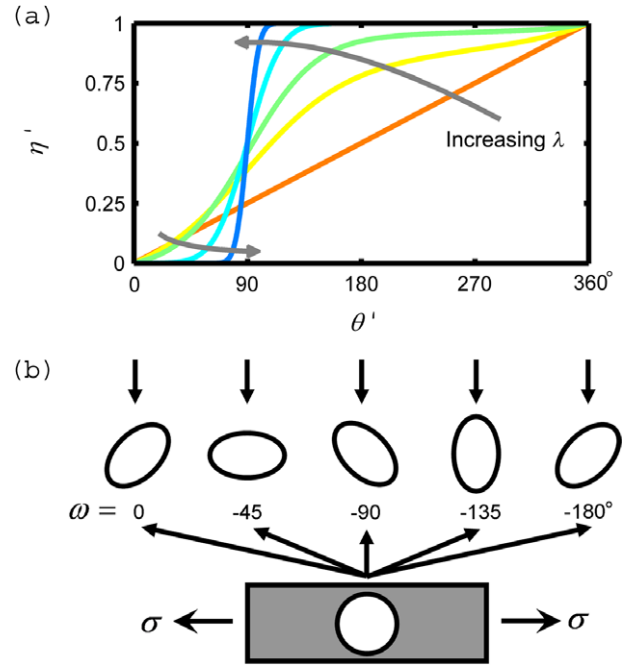


Fig. 4. (a) Evaluation of Eq. (12) as a function of θ' , in degrees, for several different values of λ . The arrows point from smaller to larger values of λ , illustrating the drive for the system to shear at the angle of maximum shear for large values of λ . (b) Illustration of the shearing of an STZ for different values of ω for a state of pure tension, where the different STZs have been lined up under part (a) to illustrate how the value of λ influences the probability of observing each type of shear event.

shearing in the direction of maximum shear. This is illustrated for the case of uniaxial tension in Fig. 4b, where $\omega = -\theta'/2$ because ϕ is zero. Several potential shear shape distortions are shown beneath Fig. 4a to illustrate how the integration limits relate to each distortion. At very high values of λ the preferred shear shape distortion is in the direction of the uniaxial tension (shear at 45° to the tensile axis) providing maximum extension for a single STZ activation.

2.3. Finite element analysis

With an ensemble of STZs defined on the mesh and the KMC algorithm to evolve the system, there remains only the matter of identifying the local states of these potential STZs, i.e. the local stress and temperature that will govern their activation. In our model, FEA is used to determine the stress and strain distributions in the system at every KMC step. When an STZ is to be activated or sheared, an increment of strain, as given in Eq. (14), can be applied to the elements belonging to that STZ and the FEA solver can then recalculate the stress and strain distributions.

For all the simulations discussed in this paper, we employ the commercial finite element package ABAQUS® as our FEA solver, with plane-strain quadratic triangular elements. We apply the STZ shearing strains through the use of ABAQUS User Subroutines, and since all plasticity occurs through these local STZ shape change events, we

only require a linear elastic solver to determine the stress and strain fields. For simplicity in this paper, we require the entire system to have a uniform temperature distribution.

We explore the issue of mesh resolution by considering the shearing of a single STZ located in the center of a triangular mesh. The analysis is performed with eight different STZ definitions, seven centered on a node and including from one to seven elements along the STZ radius, as well as a 13-element STZ centered on an element; some of these STZ definitions are shown in Fig. 2a. In each of the eight cases, the STZ is sheared in a variety of different directions to obtain a measure of error on the calculation. As this situation closely resembles the Eshelby inclusion problem [3,37], we use the analytical solution obtained by Eshelby for shearing of a circular long fiber in a matrix (plane strain) as a point of comparison. The percent error of the calculation relative to the Eshelby solution (based on the total system strain energy) is plotted in Fig. 5 as a function of the size of the STZ relative to the mesh. As these data show, convergence is achieved quite quickly, with STZs containing 13 or more elements exhibiting about 1.5% error or less. However, each time the number of elements along the STZ radius is doubled, it quadruples the number of elements required to simulate the same system size, and thus roughly quadruples the computational time; accordingly, we identify the 13-element STZ as a reasonable compromise between accuracy and computational speed. All the computations described in the remainder of this paper are carried out with 13-element STZs defined on an irregular triangular mesh, as schematically illustrated in Fig. 2b. (For comparison, we also conducted many simulations using the 6-element STZs, which gave the same results as those provided in this paper for the 13-element STZs, both in a qualitative and quantitative sense.)

It is important at this point to discuss mesh distortion that can occur through severe deformation, which leads to errors in the solutions of the stress and strain distributions. This problem can be circumvented by periodically checking for distortion of the mesh and remeshing if necessary, which requires mapping the elastic fields onto the new

Table 1

List of material properties for Vitreloy 1, $\text{Zr}_{41.2}\text{Ti}_{13.8}\text{Cu}_{12.5}\text{Ni}_{10}\text{Be}_{22.5}$.

Property	Value	Reference
μ_0	37 GPa	[47]
$d\mu/dT$	-4.0×10^{-3} GPa K ⁻¹	[47]
ν	0.352	[47]
θ_D	327 K	[48]
Ω_0	0.8 nm ³	[13]
Number of atoms in Ω_0	42	

mesh. Solution mapping can contribute to error accumulation as well, so it is important to take care that the error accumulated by solution mapping is smaller than that accumulated by simply ignoring the mesh distortion. In this paper, we limit our discussion to cases in which the mesh distortion was sufficiently low that there is no concern about the solution accuracy. However, remeshing is, in general, an important aspect of our modeling approach, especially for situations involving localization.

2.4. Material properties

Our model requires several material properties including Poisson's ratio, ν , and the temperature-dependent shear modulus, $\mu(T)$, which is defined relative to its value, μ_0 , at $T = 0$ K as

$$\mu(T) = \mu_0 + \frac{d\mu}{dT}T. \quad (16)$$

For the sake of simplicity, we neglect the abrupt changes in modulus which are experimentally observed near the glass transition temperature, and assume the linear relationship above to be valid over the range of temperatures considered in this paper. The Debye temperature, θ_D , of the material, which is related to the Debye frequency, is required for the rate calculations. Finally, two geometrical properties of the STZs are required: the STZ volume Ω_0 and the number of atoms in that volume based upon the material chemistry. In this paper, we have used material properties derived from experiments on Vitreloy 1, $\text{Zr}_{41.2}\text{Ti}_{13.8}\text{Cu}_{12.5}\text{Ni}_{10}\text{Be}_{22.5}$, as listed in Table 1. In addition, we take the value of $\hat{\tau}$, from Eq. (1), to be equal to the athermal shear stress.

3. Model output

To demonstrate the ability of this modeling framework to simulate the wide range of behaviors exhibited by glasses, we perform a series of simulations on a plane strain two-dimensional irregular triangular mesh based on 13-element STZs. Using the material properties from Table 1, this domain has approximate dimensions of 27.6 nm wide by 45.8 nm tall. In all cases the mesh is subjected to boundary conditions in which top and bottom surfaces are constrained in the y-direction and the bottom left node is fixed.

In order to implement the framework in a computationally efficient manner, we have integrated several different

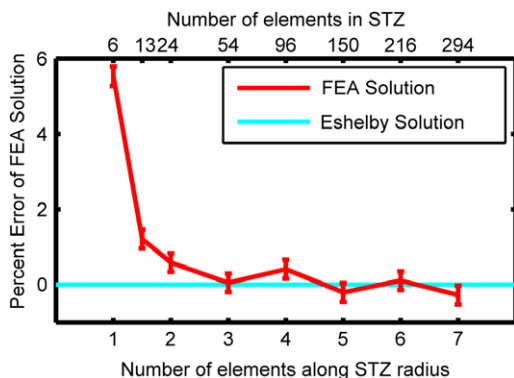


Fig. 5. Plot of the percent error between the strain energy determined by FEA methods and the Eshelby solution as a function of the size of the STZ.

software packages and coding languages. MATLAB[®] is used as a wrapper to control and call the different packages and processes; MySQL[®] is used for efficient data storage and data recall; Python is used to interact with ABAQUS CAE; FORTRAN is used to code the User Subroutines in ABAQUS; and C++ is used to post process the ABAQUS output files. Finally, the parallel processing capabilities of ABAQUS are employed to reduce the computation time of the simulations.

3.1. Thermal response and processing

We begin by first studying the effects of processing of a metallic glass by applying various thermal loads in the absence of external forces, and allowing the system to relax through sequential STZ operations. Two types of thermal response tests are performed: (i) equilibration (relaxation of the glass) at a fixed temperature; and (ii) cooling simulations where the glass is relaxed over a finite time determined by an applied cooling rate in the range 10^1 – 10^4 K s^{−1}. All the thermal response simulations are started from a system which is first equilibrated at a temperature of 1000 K, which is just above the melting temperature of Vitreloy 1 at 993 K [5].

We begin by first examining the results of our equilibration simulations. Fig. 6a shows the characteristic relaxation curves obtained in these simulations, where the instantaneous elastic strain energy density in the system is plotted as a function of time. The use of a semi-log scale permits all the equilibration curves to be presented on a single figure, but renders it difficult to clearly observe that each of the systems has actually reached an equilibrated state. An example demonstrating the convergence to a steady-state value is shown for the simulation at 400 K in the inset of Fig. 6a; all of these simulations show a similar convergence when plotted on linear time scales or as a function of the KMC time steps.

In Fig. 6a, all of the data shown are for equilibration at temperatures below the 1000 K starting state, and thus all the simulations shown involve an energy reduction. However, the steady state is independent of prior history, and the equilibrated elastic strain energy density is in fact a simple function of temperature. We find that the elastic strain energy density is proportional to the temperature with a slope of 5.27×10^{-4} eV nm^{−3} K^{−1}. This linear trend is shown over a small range of temperatures in Fig. 6b, but remains linear for the range of temperatures simulated in this paper, and in principle remains linear to 0 K.

We now turn to the data obtained in the fixed cooling rate simulations, which are shown in Fig. 6b. Here each curve represents the average of three simulations at the same cooling rate, and plots the average elastic strain energy density of the system as a function of temperature. As expected, the cooling experiments tend to track the equilibrium condition reasonably closely at first, until the temperature falls below a certain point; with further cooling the elapsed time of each KMC step rises quickly, and the system becomes kinetically trapped. The magnitude of relaxation achieved is greater

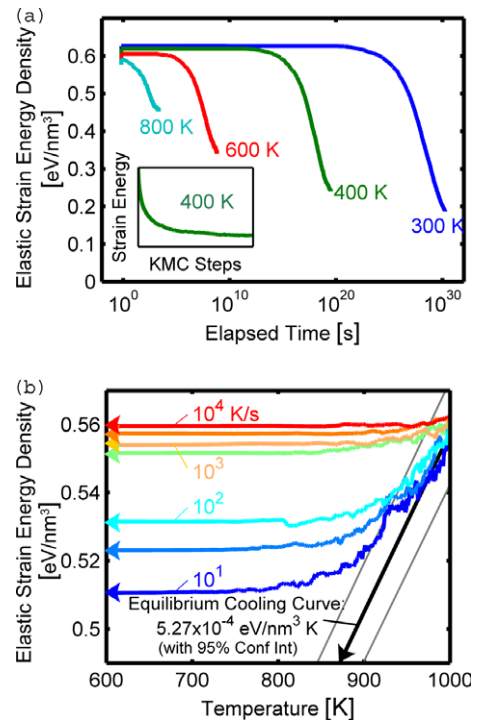


Fig. 6. (a) Plot of elastic strain energy density as a function of elapsed time for simulated equilibration of a metallic glass at different temperatures. The semi-log scale allows comparison of the different simulations but obscures the convergence of the value to a steady state, which is shown in the inset for linear axes. (b) Plot of elastic strain energy density as a function of temperature for simulated cooling of a metallic glass at different rates (10^1 , 5×10^1 , 10^2 , 5×10^2 , 10^3 , 5×10^3 , 10^4 K s^{−1}), where each curve represents the average of three simulations. In addition, the equilibrium cooling curve is plotted for comparison, which remains linear to room temperature and in principle to 0 K.

for the slower cooling rates, in which a larger number of STZ operations are allowed.

It is interesting to note that the KMC approach, by permitting arbitrarily long time scales, can yield states not seen in experiments or other simulations. For example, our equilibrium elastic strain energy density trend in Fig. 6b differs from prior suggestions that the energy associated with the fluctuations of atomic level stresses should depart from linearity for values below the glass transition temperature, T_g [17,19,43]. While such a departure from linearity is clearly possible when short time scales produce kinetically metastable structures (as in our cooling simulations in Fig. 6b), the KMC algorithm allows the system to visit states that would not be accessible on reasonable time scales, e.g. 10^{30} s (cf. Fig. 6a). Thus, in our equilibrated structures we observe a linear reduction of system energy as temperature decreases well below T_g .

3.2. High-temperature rheology

The high-temperature deformation of a metallic glass provides a convenient validation point for our model, since at sufficiently high temperatures (small λ), thermal energy dominates STZ activation, the local stress state becomes

less important and STZs are expected to act essentially independently of one another. Under such conditions, an analytical expression for the glass rheology is possible.

In the classical one-dimensional model, STZs may shear either forward or backward, and combining the rates of these two processes yields the following hyperbolic-sine stress-dependent phenomenology in the steady state [3,44]:

$$\dot{\gamma} = 2 \cdot \gamma_o \cdot v_o \cdot \exp\left(-\frac{\Delta F}{kT}\right) \cdot \sinh\left(\frac{\tau \cdot \gamma_o \cdot \Omega_o}{kT}\right), \quad (17)$$

where $\dot{\gamma}$ is the shear strain rate. This approach is readily expanded to a two-dimensional case where STZs can shear in any direction in the plane, which is more relevant for comparison with our model. In this situation the average strain rate is found by considering the contribution of strain from shearing an STZ in any direction around the orientation circle. The derivation is very similar to that used to obtain Eq. (4), and yields:

$$\dot{\gamma} = 2\pi \cdot \gamma_o \cdot v_o \cdot \exp\left(-\frac{\Delta F}{kT}\right) \cdot I_1\left(\frac{\tau \cdot \gamma_o \cdot \Omega_o}{kT}\right), \quad (18)$$

where I_1 is a modified Bessel function of the first kind, of order one. Eqs. (17) and (18) predict remarkably similar strain rates for the same temperature and stress, with only subtle differences between them. For example, at low stresses, Eq. (18) predicts a slightly faster strain rate (by a factor of ~ 2.2 at 50 MPa and T_g) because the extra degrees of freedom allow STZs that shear at off-angles to contribute to the forward strain rate. At high stresses, however, the extra degrees of freedom in Eq. (18) actually predict a slower strain rate (by a factor of ~ 0.27 at 1 GPa and T_g) than Eq. (17) because the off-angle STZ shearing events predict a slower strain rate than having all forward flips as in the one-dimensional model.

We study the rheological behavior of our simulated glass over a range of stresses at different constant temperatures near and above 623 K, the glass transition temperature of Vitreloy 1 [5]. We explore deformation in three different classes of structures:

- *Equilibrated structures*, which are first equilibrated without an applied load at the test temperature, followed by application of a load at the same temperature.
- *Cooled structures*, which are cooled from the equilibrated structure at 1000 K at a rate of 10 K s^{-1} to 300 K (cf. Fig. 6b) prior to the application of a load at a different temperature.
- *Unequilibrated structures*, which comprise an undeformed mesh, free from any prior STZ operations, with no internal stress distribution prior to loading at the test temperature.

In all cases, temperature and stress (in a loading state of pure shear, with displacement along the x -axis) are fixed at constant values, and the KMC algorithm evolves the system through sequential STZ operations.

Typical shear strain–time data for the three different structures are shown in Fig. 7a for a load of 400 MPa at

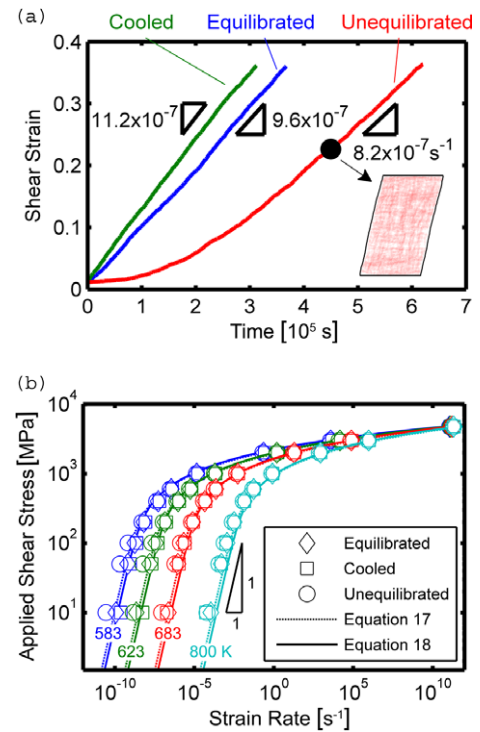


Fig. 7. (a) Typical strain–time data for the three different structures deformed at high temperatures (in this case 400 MPa and 623 K), which exhibit similar steady-state strain rates and overall shear strain. A snapshot is provided for the unequilibrated structure at the marked point, where the inset shows the physical deformation along with the magnitude of the plastic STZ strains, which are shaded. (b) Steady-state homogeneous flow data for several high temperature simulations of the three structures, plotted along with the predicted strain rates of Eqs. (17) and (18).

623 K. The responses for the cooled and equilibrated structures are very similar, exhibiting almost instantaneously a constant steady-state strain rate. On the other hand, the unequilibrated structure exhibits a significant transient region, during which the structure is developing the beginnings of a steady-state internal stress distribution that permits more rapid deformation; the first few STZ operations are large perturbations in the unequilibrated system, and require longer times to occur. After the conclusion of the transient, however, the steady-state strain rate is essentially the same as that seen in the other two structures. The deformation in all the structures is also uniform, or homogeneous in nature, as expected. An illustration of the observed deformation is provided for the unequilibrated structure at a time intermediate to the final deformation, with the magnitude of the STZ strains shaded, which can be seen in the inset of Fig. 7a. All the high temperature deformation tests showed a similar uniform distribution of STZ strains and homogeneous deformation.

The steady-state strain rates of all three structures are plotted in Fig. 7b as a function of the applied load for a variety of test temperatures. As expected based on the discussion above, all three structures exhibit similar rheology in the steady-state condition. What is more, the shape of

the datasets in Fig. 7b is typical of homogeneous glass flow, exhibiting weakly rate-dependent near-Newtonian flow at low stresses, and a gradual increase in rate sensitivity with increasing stress. The predictions of Eqs. (17) and (18) are also plotted in Fig. 7b, both of which agree closely with the simulation results without the use of any adjustable parameters; this close agreement suggests that the assumption of independent STZ operation is well founded at these temperatures near the glass transition. We also observe that while the two-dimensional model of Eq. (18) does provide somewhat improved predictions in some cases, the simpler one-dimensional model of Eq. (17), with its classical hyperbolic-sine stress dependence, provides surprisingly accurate results with an error on average $\sim 5\%$ smaller than Eq. (18).

3.3. Low-temperature deformation

We now consider deformation of the same three structures at two temperatures, 300 and 400 K, well below the nominal glass transition temperature of Vitreloy 1 at 623 K. Typical strain–time data are shown in Fig. 8a for the three different structures loaded at 1 GPa and 300 K, where it can be seen that once a certain strain level is achieved, all three structures exhibit about the same strain rate. However, the three different structures exhibit very different initial responses to the applied load, where the cooled structure shows no transient region, the equilibrated structure shows a small transient region and the unequilibrated structure once again shows a very significant transient region. The lack of a transient in the cooled structure can be attributed to the higher strain energy density that is frozen into the system, which is ~ 2.5 times greater than the strain energy density in the equilibrated structure. Thus, in comparing the cooled and equilibrated structures, the higher stresses in the cooled structure make it more readily able to deform than the equilibrated structure, which requires a transient region to initiate rapid deformation.

The significant transient region in the unequilibrated structure can again be attributed to the development of an internal stress distribution that facilitates deformation, where the first STZ operations represent large perturbations to the system that require a long time to occur. What is more, these first few STZs are spatially clustered, as shown in Fig. 8b, and ultimately assemble into the nucleus of a shear band as in Fig. 8c. Once this assemblage of STZs spans the specimen as in Fig. 8c, the stress state of the system is sufficiently perturbed to permit rapid shearing on this plane, which accumulates strain quickly as in Fig. 8d.

At low temperatures and high loads (large λ), a glass generally deforms inhomogeneously with the majority of plastic strain confined to very localized volumes, exactly as seen in the example of Fig. 8b–d. However, while this behavior was observed in the unequilibrated structure, the equilibrated and cooled structures deformed in a homogeneous fashion with no sign of localization in over 40 unique simulations, despite identical loading conditions.

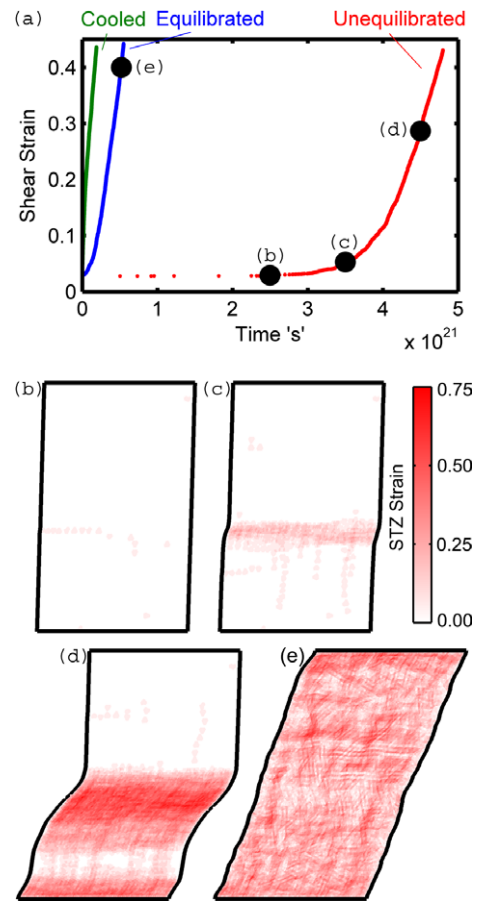


Fig. 8. (a) Typical strain–time data for the three different structures deformed at low temperatures (in this case 1 GPa and 300 K), which exhibit similar steady-state strain rates and overall shear strain although they exhibit different transients. Markers (b), (c) and (d) correspond to snapshots of the unequilibrated structure at different times during deformation, illustrating the localization into an elementary shear band. Marker (e) corresponds to a single snapshot of the equilibrated structure near the end of loading illustrating the homogeneous nature of the deformation.

This homogeneity (or lack of inhomogeneity) in the equilibrated and cooled structures can, we believe, be attributed to the system size; the small physical size of the simulation cell falls in the reported range of the width of a fully developed shear band at 10^{-8} – 10^{-7} m [7,8]. This may simply be too small to allow a shear band to develop in the complex stress field of an amorphous solid. The localization of the stress and strain distributions which give rise to shear banding requires a perturbation of sufficient size. In the unequilibrated structure, the perturbation is provided by thermal activation of the first few STZs, which generate stress and strain distributions of a large magnitude in an otherwise stress free mesh. Subsequent STZs are strongly biased by the perturbation, leading to the autocatalytic assembly of a shear band as in Fig. 8b–d. However, in the systems with pre-existing structural noise, a single STZ operation does not provide a sufficient perturbation to trigger shear banding, because stresses of similar magni-

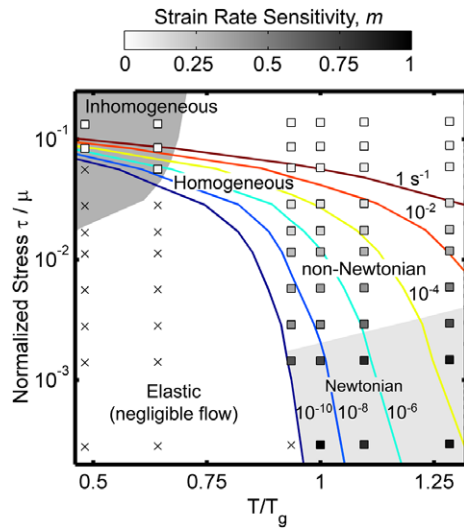


Fig. 9. A deformation map for Vitreloy 1 constructed from data obtained from loading the unequilibrated structure over a range of loads and temperatures. The colored lines represent contours of different steady-state strain rates, where strain rates slower than 10^{-10} s^{-1} are considered to be elastic and are marked with an “x”. Other data points are shaded according to their respective strain rate sensitivity, m , as indicated by the color bar above the map. Further regions marked as Newtonian (lightly shaded) and non-Newtonian are differentiated. Samples which deformed inhomogeneously are marked in a darkly shaded region while the rest of the samples deformed homogeneously.

tude are already distributed through the system; a larger perturbation is apparently required, involving multiple STZ operations. In a small system such as ours, the probability for observing a perturbation of sufficient size is reduced. The role of large stress fluctuations inhibiting inhomogeneous deformation has been explored previously in Ref. [45] with a different model, and similar physics may be at work here.

In future work we will explore in more detail the conditions required to cause localization in these simulations. In addition to issues of scale, we also intend to incorporate local state variables, including structural parameters (such as free volume) and local temperature; these will permit additional perturbations in the local state and are known to generally lead to (or influence) localization [4].

3.4. Deformation map

As a final illustration of the general capabilities of this model, we assemble in Fig. 9 a deformation map derived from simulations on the unequilibrated structure. The map includes:

- Contours of steady-state strain rate as a function of temperature and stress, for rates ranging from 10^{-10} to 1 s^{-1} . The material response at strain rate values slower than 10^{-10} s^{-1} is assigned as nominally “elastic”; these data points are marked by an x rather than a square.

- Local values of the strain rate sensitivity, m , defined as

$$m = \frac{d \ln \tau}{d \ln \dot{\gamma}} \quad (19)$$

As the stress is increased, the value of m decreases from unity (Newtonian flow), and trends toward zero, which is associated with non-Newtonian flow and instabilities [46].

- Regions to denote which samples deformed in a homogeneous manner and which samples deformed in an inhomogeneous manner.

The general features of the deformation map match well with expectations for metallic glasses [1,44]. With the ability to reproduce the basic features of glass deformation, we anticipate that the present STZ-dynamics model will be able to shed new light on more obscure details of deformation that are not captured on the deformation map.

4. Conclusions

We have developed a new mesoscale modeling technique for the mechanical behavior of metallic glasses, based on shear transformation zone dynamics. The important features of this modeling framework include the following:

- A model material is coarse-grained and mapped onto a mesh to form an ensemble of shear transformation zones (STZs), which are the fundamental units of plastic deformation.
- Finite element analysis and a kinetic Monte Carlo algorithm are used together in this model, the former to permit STZs to interact via their stress and strain fields, and the latter to permit time evolution of the ensemble.

The result is a model that can access significantly larger time and length scales than those typically available via atomistic modeling, with complex geometries and boundary conditions. These larger time and length scales are necessary to understand how microscopic deformation leads to macroscopically and experimentally observed behaviors.

We have presented a specific implementation of the modeling technique in two dimensions, to model a metallic glass over a range of thermal conditions and mechanical loads. Salient results from this exercise include the following:

- In equilibrium, there is a linear relationship between the stored elastic strain energy density and temperature. Cooling the system at a finite rate leads to a deviation from equilibrium and the entrapment of a kinetically metastable state with higher stored elastic strain energy density.
- Deformation of the system at high temperatures and at a constant load leads to steady-state strain rates regardless of the processing history (pre-existing internal stress distributions), although the processing history can affect the transient approach to a steady state. The steady-

state rheology conforms well to simple analytical models that assume independence of STZs from one another. Both Newtonian and non-Newtonian flows are observed, in line with expectations.

- While deformation at high temperatures is observed to be homogeneous, at low temperatures inhomogeneous flow (i.e. shear banding) is observed in initially noise-free (unequilibrated) structures. In such systems, the first STZs that operate provide a perturbation that leads to autocatalytic shear band assembly. In contrast, systems with a thermal/processing history with significant pre-existing internal stress distributions deform in a homogeneous manner.

With the results obtained from numerous simulations, we assembled a deformation map for metallic glasses that is in line with expectations from the literature. It is expected that our STZ dynamics model can be applied to understand more subtle details of glass deformation under complex boundary conditions and at large scales.

Acknowledgments

This work was primarily supported by the Office of Naval Research (ONR) under Contract No. N00014-08-1-0312. E.R.H. gratefully acknowledges fellowship support through the National Defense Science and Engineering Graduate (NDSEG) Fellowship with support from the Army Research Office (ARO).

References

- [1] Schuh CA, Hufnagel TC, Ramamurty U. *Acta Mater* 2007;55:4067.
- [2] Johnson WL. *JOM-J Miner Met Mater Soc* 2002;54:40.
- [3] Argon AS. *Acta Metall* 1979;27:47.
- [4] Falk ML, Langer JS. *Phys Rev E* 1998;57:7192.
- [5] Lu J, Ravichandran G, Johnson WL. *Acta Mater* 2003;51:3429.
- [6] Barrat JL, de Pablo JJ. *MRS Bull* 2007;32:941.
- [7] Neuhauser H. *Scripta Metall* 1978;12:471.
- [8] Hufnagel TC, Jiao T, Li Y, Xing LQ, Ramesh KT. *J Mater Res* 2002;17:1441.
- [9] Donovan PE, Stobbs WM. *Acta Metall* 1981;29:1419.
- [10] Pekarskaya E, Kim CP, Johnson WL. *J Mater Res* 2001;16:2513.
- [11] Conner RD, Li Y, Nix WD, Johnson WL. *Acta Mater* 2004;52:2429.
- [12] Conner RD, Johnson WL, Paton NE, Nix WD. *J Appl Phys* 2003;94:904.
- [13] Fu XL, Li Y, Schuh CA. *J Mater Res* 2007;22:1564.
- [14] Zink M, Samwer K, Johnson WL, Mayr SG. *Phys Rev B* 2006;73:3.
- [15] Albano F, Falk ML. *J Chem Phys* 2005;122:8.
- [16] Srolovitz D, Maeda K, Vitek V, Egami T. *Philos Mag A* 1981;44:847.
- [17] Chen SP, Egami T, Vitek V. *Phys Rev B* 1988;37:2440.
- [18] Vitek V, Egami T. *Phys Stat Solidi B* 1987;144:145.
- [19] Egami T, Srolovitz D. *J Phys F* 1982;12:2141.
- [20] Deng D, Argon AS, Yip S. *Philos Trans R Soc Lond Ser A* 1989;329:549.
- [21] Deng D, Argon AS, Yip S. *Philos Trans R Soc Lond Ser A* 1989;329:575.
- [22] Deng D, Argon AS, Yip S. *Philos Trans R Soc Lond Ser A* 1989;329:595.
- [23] Deng D, Argon AS, Yip S. *Philos Trans R Soc Lond Ser A* 1989;329:613.
- [24] Shi YF, Falk ML. *Phys Rev B* 2006;73:10.
- [25] Lund AC, Schuh CA. *Acta Mater* 2003;51:5399.
- [26] Falk ML. *Phys Rev B* 1999;60:7062.
- [27] Bailey NP, Schiotz J, Jacobsen KW. *Phys Rev B* 2006;73:12.
- [28] Shi Y, Falk ML. *Scripta Mater* 2006;54:381.
- [29] Shi YF, Falk ML. *Phys Rev Lett* 2005;95:4.
- [30] Shi YF, Falk ML. *Appl Phys Lett* 2005;86:3.
- [31] Shi YF, Falk ML. *Acta Mater* 2007;55:4317.
- [32] Su C, Anand L. *Acta Mater* 2006;54:179.
- [33] Thamburaja P, Ekambaram R. *J Mech Phys Solids* 2007;55:1236.
- [34] Bulatov VV, Argon AS. *Model Simul Mater Sci Eng* 1994;2:167.
- [35] Bulatov VV, Argon AS. *Model Simul Mater Sci Eng* 1994;2:185.
- [36] Bulatov VV, Argon AS. *Model Simul Mater Sci Eng* 1994;2:203.
- [37] Eshelby JD. *Proc R Soc Lond Ser A* 1957;241:376.
- [38] Argon AS, Shi LT. *Acta Metall* 1983;31:499.
- [39] Argon AS, Kuo HY. *Mater Sci Eng* 1979;39:101.
- [40] Srolovitz D, Vitek V, Egami T. *Acta Metall* 1983;31:335.
- [41] Voter A. In: Sickafus KK, Kotomin EA, Uberuaga BP, editors. *Proceedings of the NATO advanced study institute on radiation effects in solids held in Erice, Sicily, Italy, vol. 235*. Berlin: Springer; 2004.
- [42] Amar JG. *Comput Sci Eng* 2006;8:9.
- [43] Vitek V, Chen SP, Egami T. *J Non-Cryst Solids* 1984;61–62:583.
- [44] Spaepen F. *Acta Metall* 1977;25:407.
- [45] Jagla EA. *Phys Rev E* 2007;76:7.
- [46] Burke MA, Nix WD. *Acta Metall* 1975;23:793.
- [47] Johnson WL, Samwer K. *Phys Rev Lett* 2005;95:4.
- [48] Wang Q, Pelletier JM, Blandin JJ, Suery M. *J Non-Cryst Solids* 2005;351:2224.